FRONTIERS OF PHYSICS

RESEARCH ARTICLE
Volume 17 / Issue 6 / 61503 / 2022

Bose–Einstein condensates with tunable spin–orbit coupling in the two-dimensional harmonic potential: The ground-state phases, stability phase diagram and collapse dynamics

Chen Jiao[1], Jun-Cheng Liang[1], Zi-Fa Yu[1], Yan Chen[2], Ai-Xia Zhang[1], Ju-Kui Xue[1,†]

1 College of Physics and Electronics Engineering, Northwest Normal University, Lanzhou 730070, China
2 School of Physics and Electromechanical Engineering, Hexi University, Zhangye 734000, China
Corresponding author. E-mail: †xuejk@nwnu.edu.cn
Received November 24, 2021; accepted May 24, 2022

© Higher Education Press 2022

ABSTRACT

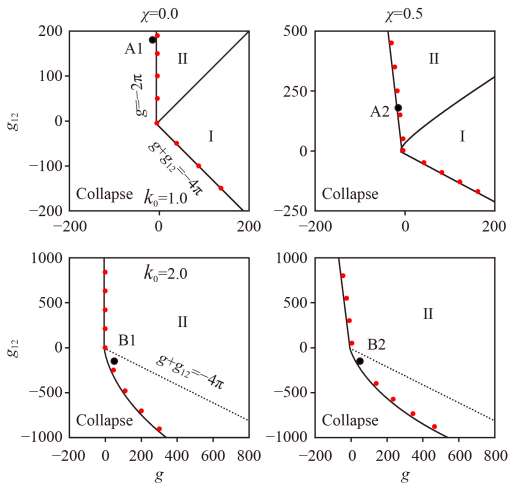

We study the ground-state phases, the stability phase diagram and collapse dynamics of Bose–Einstein condensates (BECs) with tunable spin–orbit (SO) coupling in the two-dimensional harmonic potential by variational analysis and numerical simulation. Here we propose the theory that the collapse stability and collapse dynamics of BECs in the external trapping potential can be manipulated by the periodic driving of Raman coupling (RC), which can be realized experimentally. Through the high-frequency approximation, an effective time-independent Floquet Hamiltonian with two-body interaction in the harmonic potential is obtained, which results in a tunable SO coupling and a new effective two-body interaction that can be manipulated by the periodic driving strength. Using the variational method, the phase transition boundary and collapse boundary of the system are obtained analytically, where the phase transition between the spin-nonpolarized phase with zero momentum (zero momentum phase) and spin-polarized phase with non-zero momentum (plane wave phase) can be manipulated by the external driving and sensitive to the strong external trapping potential. Particularly, it is revealed that the collapsed BECs can be stabilized by periodic driving of RC, and the mechanism of collapse stability manipulated by periodic driving of RC is clearly revealed. In addition, we find that the collapse velocity and collapse time of the system can be manipulated by periodic driving strength, which also depends on the RC, SO coupling strength and external trapping potential. Finally, the variational approximation is confirmed by numerical simulation of Gross–Pitaevskii equation. Our results show that the periodic driving of RC provides a platform for manipulating the ground-state phases, collapse stability and collapse dynamics of the SO coupled BECs in an external harmonic potential, which can be realized easily in current experiments.

Keywords spin–orbit coupled Bose–Einstein condensates, stability, collapse dynamics

1 Introduction

The laboratory realization of ultracold neutral atomic gases such as Bose–Einstein condensates (BECs) [1–3] and degenerate Fermi gases [4, 5] – quantum gases – provide an ideal experimental platform to simulate the various phenomena of the condensate physics [6]. However, in the experiment, the collapse stability of the condensates plays an important role in the realization and application of BECs. In the free space, for three

https://doi.org/10.1007/s11467-022-1180-3

dimensional (3D) BECs, the collapse, where the size of the condensates decreases to zero after a finite time, occurs at any attractive atomic interaction strength [7]; while it occurs only at a strong enough attractive atomic interaction for two dimensional (2D) case [8–10]. The presence of trapping potential allows one to achieve metastable BECs for weaker attractive interaction if the number of particles N is less than a certain number N_c [11], because the atoms can gain zero-point energy to balance the attractive interaction when they are spatially confined [8]. Thus, the BECs stability depends on the interatomic interaction, the trapping potential and the geometric dimension of the system [11, 12]. The interatomic interactions are composed of dominant isotropic short-range contact interaction and anisotropic long-range dipole–dipole interaction. Due to a very large particle wavelength compared with the atomic radius, the interatomic interaction can be accurately described by a single parameter, the scattering length a_s, where positive (negative) a_s corresponds to repulsion (attraction) between the atoms, and the sign and the amplitude of a_s can be modulated by Feshbach resonance technique [13–15]. Thus, the collapse can be controlled by temporal modulation of the scattering length [16–18]. When dipole interactions are considered, the stability and collapse of the BECs strongly depend on cloud anisotropy [12, 19].

The BECs physics has been more enriched and extensively studied with the realization of the synthetic gauge fields [20, 21] and the synthetic spin–orbit (SO) coupling [22–26]. In particular, the SO coupling affects the ground-state properties of the BECs [27–30] and maintains the stability of the system [31–36], which is due to the linear SO coupling term breaking the Galilean invariance, resulting in the stabilization of the system [31, 32, 37, 38]. In 2D free space, the stable 2D composite solitons in the BECs are generated by SO coupling and attractive atomic interaction [31]. In the context of binary BECs with contact self-attraction and SO coupling, the existence of metastable solitons in 3D free space is proved [33]. The collapse theory of SO coupled BECs is proposed in free space [34] and external trapping potential [35], respectively. Unfortunately, the SO coupling strength in most experiments and theoretical work is not tunable because it is determined by the directions and wavelengths of the Raman laser. Hence, how to control the stability of the condensates by the SO coupling is still an open subject.

In recent years, the extensive attention has been devoted to the Floquet engineering in the various quantum systems [39] due to its ability to generate new interactions [40, 41], which is also widely applied in periodically driven cold atom systems [42–50]. In cold atom physics, the BECs with tunable SO coupling have been achieved by fast coherent modulation of Raman laser intensity in the experiments [42, 43], which provides a powerful tool for exploring new physical phenomenon. Subsequently, the heating mechanism of this experimental scheme is analyzed, and it is shown that the periodic driving of Raman coupling (RC) is still reasonable when the driving strength is large enough [44]. The tunable SO coupling leads to richer physical phenomena, such as the controllable localization properties of the ground state in deep lattices [45], the controllable dynamics of solitons and Josephson-type oscillations between soliton components [46], and the generation of a robust magnetic superstripe phase [47]. Recently, the ground-state phases and superfluidity of BECs with tunable SO coupling in free space are studied, and they found that the phase transition and the sound velocity of the system can be regulated by external driving [48]. According to experimental parameters, phase diagrams of ^{87}Rb and ^{23}Na BECs with tunable SO coupling are given in free space [49]. However, the external trapping potential exists in the real experimental system, and the collapse stability of the ground-state phases of the BECs with tunable SO coupling and external trapping is not considered. Thus, the aim of the present paper is to investigate the manipulating of the stability of SO coupled BECs by periodic driving of RC in a harmonic potential, which is consistent with real experiments.

The paper is organized as follows. In Section 2, based on the model of BECs with tunable SO coupling, the effective time-independent Floquet Hamiltonian is obtained through an appropriate unitary transformation and the high frequency approximation. In Section 3, according to the band structure of the system, we find that the periodic driving of RC can control the phase transition and stability of the system, and the phase transition boundary of the system is obtained by the variational method. In Section 4, according to the phase transition conditions, the effect of the periodic driving strength on the phase transition is studied. We find that, with the increasing of periodic driving strength χ, the phase transition from the plane wave phase to the zero momentum phase occurs, which is more obvious in the case of strong harmonic potential or repulsive interspecies interaction. Similarly, the influence of the periodic driving strength on the stability phase diagram is studied through the obtained collapse boundary, which forms the Section 5. Particularly, the mechanism of collapse stability manipulated by periodic driving of RC is clearly revealed. The effect of the periodic driving strength on collapse dynamics is shown in Section 6. We find that the collapse velocity and collapse time can be manipulated by periodic driving strength, which also depends on the RC, SO coupling strength and external trapping potential. In this section, the variational approximation is verified by numerical simulation of the Gross–Pitaevskii (G–P) equation. Finally, The paper is summarized in Section 7.

2 The model

Based on the experimental realization of SO coupling in BECs reported in Refs. [22, 42, 43], we consider a pancake-shaped two-component BECs of pseudospin-1/2 particles with equal Rashba and Dresselhaus contributions for SO coupling terms, loaded into an external two-dimensional harmonic potential. In the framework of the mean-field approximation, the system can be described by a dimensionless Hamiltonian [11, 21, 42, 43]

$$H = H_0 + H_{int}, \tag{1}$$

where

$$H_0 = \frac{1}{2}[(p_x - k_0\hat{\sigma}_z)^2 + p_y^2] + \frac{\Omega}{2}\hat{\sigma}_x + \frac{\delta}{2}\hat{\sigma}_z + V_{ext} \tag{2}$$

is the dimensionless single-particle Hamiltonian. Here, $p_x = -\mathrm{i}\partial/\partial x$ and $p_y = -\mathrm{i}\partial/\partial y$ are the atomic momentum operator in the x direction and y direction, respectively. $\hat{\sigma}_i$ are Pauli matrices. $k_0 = \tilde{k}_0/(\hbar l_z^{-1})$ is the dimensionless SO coupling strength. $\Omega = \tilde{\Omega}/(\hbar\omega_z)$ is the dimensionless Raman coupling (RC) strength. $\delta = \tilde{\delta}/(\hbar\omega_z)$ is the dimensionless two-photon detuning. $l_z = \sqrt{\hbar/(m\omega_z)}$ is the characteristic length of the condensates with external trapping frequency ω_z in the z direction, with m being the atomic mass. $V_{ext} = \omega^2(x^2 + y^2)/2$ is the external harmonic potential with $\omega = \omega_\perp/\omega_z$, and $\omega_\perp$ is the trapping frequency in the transverse plane.

The dimensionless interatomic two-body interaction H_{int} can be written as [11, 33]

$$H_{int} = \mathrm{diag}(g_{11}|\Phi_1|^2 + g_{12}|\Phi_2|^2, g_{22}|\Phi_2|^2 + g_{12}|\Phi_1|^2), \tag{3}$$

where Φ_1 and Φ_2 are the condensates wave functions describing the two pseudospin components interacting with the coupling constants $g_{ij} = 2\sqrt{2\pi}N\hbar a_{ij}/(m\omega_z l_z^3)$, where N is the total number of atoms and a_{ij} are the corresponding interatomic s-wave scattering lengths. According to the experiments [22], we can take $\omega_z \sim 1$ kHz and $N \sim 10^5$, meanwhile a_{ij} can be adjusted up to $10^3\, a_0$ and g_{ij} can be up to 10^4 by Feshbach resonance technology, where a_0 is Bohr radius.

Unfortunately, in the experiment, the SO coupling strength is not tunable because the SO coupling strength is determined by the directions and wavelengths of the Raman lasers. Now, we consider the case that the SO coupling strength can be controlled by modulating the RC strength in the form [42–45]

$$\Omega \to \Omega(t) = \Omega_0 + \Omega_R \cos(\omega_R t), \tag{4}$$

where Ω_0 denotes the fixed constant part of the RC strength, Ω_R is the modulation amplitude and ω_R is the modulation frequency.

According to the experiments [42, 43], in order to achieve the adjustable SO coupling, the RC strength can be adjusted in real time by controlling the intensity and phase of the Raman laser. In the experimental scheme, when $\Omega_R > \Omega_0$, the sign of Ω at a certain time can be changed by applying a π phase shift on one Raman laser [42, 43]. Meanwhile, the modulation frequency ω_R is required to be much larger than other energy scales in the system (i.e., the driven frequency ω_R is of the order of kHz). In such high frequency cases, the time-dependent modulation term in the RC strength can be eliminated by the high-frequency approximation method, and the time-independent Floquet Hamiltonian of the system can be obtained. In order to analyze the dynamics resulting from the driving, we introduce the following unitary transformation [42, 44]:

$$U(t) = \exp\left[-\mathrm{i}\frac{\Omega_R \sin(\omega_R t)}{2\omega_R}\hat{\sigma}_x\right]. \tag{5}$$

The transformed two-component wave function is $\Psi = U^\dagger\Phi$ with $\Psi = (\psi_1, \psi_2)^{\mathrm{T}}$. After using the Floquet theory $H_F = H(t) - \mathrm{i}\hbar\partial_t$ [40], the transformed Hamiltonian can be written as

$$H' = U^\dagger(H_0 + H_{int})U - \mathrm{i}U^\dagger\frac{\partial U}{\partial t}. \tag{6}$$

In order to obtain the time-independent Hamiltonian, the time-varying part of the transformed Hamiltonian Eq. (6) can be eliminated by the following integral:

$$\bar{H}_{\mathrm{eff}} = \int_0^\tau H'\mathrm{d}t = \bar{H}_0^{\mathrm{eff}} + \bar{H}_{int}^{\mathrm{eff}}, \tag{7}$$

where $\tau = 2\pi/\omega_R$ is the modulation period of the RC constant and $\bar{H}_{\mathrm{eff}}$ is the effective time-independent Floquet Hamiltonian of the system. $\bar{H}_0^{\mathrm{eff}}$ and $\bar{H}_{int}^{\mathrm{eff}}$ are effective single-particle Hamiltonian and two-body interaction Hamiltonian, respectively. The effective single-particle Hamiltonian becomes

$$\begin{aligned}\bar{H}_0^{\mathrm{eff}} =& \frac{1}{2}(p_x^2 + p_y^2 + k_0^2) - J_0(\chi)k_0 p_x\hat{\sigma}_z \\ &+ \frac{\Omega_0}{2}\hat{\sigma}_x + \frac{\delta}{2}J_0(\chi)\hat{\sigma}_z + V_{ext},\end{aligned} \tag{8}$$

where $J_0(\chi)$ is the zeroth-order Bessel function of the first kind and $\chi = \Omega_R/\omega_R$ is the periodic driving strength of RC. Eq. (8) indicates that the effective SO coupling strength $J_0(\chi)k_0$ is generated by the periodic driving of RC, which means a tunable SO coupling is realized.

In addition, the effective two-body interaction Hamiltonian becomes

$$\bar{H}_{int}^{\mathrm{eff}} = \begin{pmatrix} g'_{11}|\psi_1|^2 + g'_{12}|\psi_2|^2 & g'_{33}(\psi_1\psi_2^* - \psi_2\psi_1^*) \\ g'_{33}(\psi_2\psi_1^* - \psi_1\psi_2^*) & g'_{12}|\psi_1|^2 + g'_{22}|\psi_2|^2 \end{pmatrix}, \tag{9}$$

where the effective interaction constants are given by

$$
\begin{aligned}
g'_{11} &= \frac{1}{8}[(3+J_0(2\chi))(g_{11}+g_{22})+2(1-J_0(2\chi))g_{12} \\
&\quad +4J_0(\chi)(g_{11}-g_{22})], \\
g'_{12} &= \frac{1}{8}[(1-J_0(2\chi))(g_{11}+g_{22})+2(3+J_0(2\chi))g_{12}], \\
g'_{33} &= \frac{1}{8}[(1-J_0(2\chi))(g_{11}+g_{22})-2(1-J_0(2\chi))g_{12}], \\
g'_{22} &= \frac{1}{8}[(3+J_0(2\chi))(g_{11}+g_{22})+2(1-J_0(2\chi))g_{12} \\
&\quad -4J_0(\chi)(g_{11}-g_{22})]. \qquad (10)
\end{aligned}
$$

Here, g'_{11}, g'_{22} and g'_{12} are the tunable strength of interatomic interaction due to period driving of RC. Meanwhile, because of the high frequency modulation, the new type of two-body interaction appears in the non-diagonal elements of the effective two-body Hamiltonian $\bar{H}^{\rm eff}_{int}$. Eq. (8) indicates that, when there is no periodic driving of RC (i.e., $\chi=0$), the effective two-body interaction Hamiltonian $\bar{H}^{\rm eff}_{int}$ is consistent with the dimensionless two-body interaction Hamiltonian H_{int}. Moreover, if the interaction Hamiltonian has $SU(2)$ spin-rotational symmetries (i.e., $g_{11}=g_{22}=g_{12}$), the two-body interaction is not affected by the spin-dependent unitary transformation, and the non-diagonal terms in Eq. (9) disappear.

3 The variational analysis

Now, we investigate the ground-state phases of BECs with tunable SO coupling in the two-dimensional harmonic potential by the variational method. According to the effective Hamiltonian Eq. (7) and mean-field method, the system's dimensionless mean-field energy functional is given by

$$
E=\int[(\psi_1^*,\psi_2^*)\left(\bar{H}^{\rm eff}_0+\frac{1}{2}\bar{H}^{\rm eff}_{int}\right)(\psi_1,\psi_2)^{\rm T}]{\rm d}\boldsymbol{r}. \qquad (11)
$$

Notice that we only consider the plane wave and zero momentum phases, and the stripe phase is ignored. Thus, the following normalized spinor Gaussian wave function is taken as the trial wave function:

$$
\begin{pmatrix}\psi_1\\ \psi_2\end{pmatrix}=\begin{pmatrix}\sqrt{1+s}\\ -\sqrt{1-s}\end{pmatrix}\frac{1}{\sqrt{2\pi}R}\cdot\exp\left(-\frac{\boldsymbol{r}^2}{2R^2}+{\rm i}\boldsymbol{k}\cdot\boldsymbol{r}\right), \qquad (12)
$$

with the wave packet width R ($R>0$), spatial coordinate $\boldsymbol{r}=(x,y)$, momentum $\boldsymbol{k}=(k_x,k_y)$, and the average spin polarization $\langle\sigma_z\rangle=s$ ($-1\le s\le 1$), which determines the spin structure of the wave function.

For simplicity, we assume a spin symmetric interaction with $g_{11}=g_{22}=g$ and $\delta=0$. Upon substituting the trial wave function into the energy functional Eq. (11), one can obtain

$$
\begin{aligned}
E=&\frac{1}{2}(k_x^2+k_y^2+k_0^2+\omega^2R^2)+\frac{1}{2R^2}-J_0(\chi)k_0k_xs \\
&+\frac{g+g_{12}}{8\pi R^2}+\frac{s^2(g-g_{12})[1+J_0(2\chi)]}{16\pi R^2} \\
&-\frac{\Omega_0}{2}\sqrt{1-s^2}. \qquad (13)
\end{aligned}
$$

Eq. (13) shows that the periodic driving modifies the SO coupled energy term and the spin-dependent interaction term of the system, which leads to the manipulation of the energy band structure of the ground state, thus the phase transition and stability diagrams of the system can be manipulated by the periodic driving.

In order to obtain the ground state of the system, we must determine the variational parameters $q_i=\{k_x,k_y,R,s\}$ by minimizing the energy functional E of the system. First, considering minimization of Eq. (13) with respect to k_x and k_y, respectively, one obtains $(k_x,k_y)=(k_m,0)$, where $k_m=J_0(\chi)k_0s$. Then, by inserting $(k_x,k_y)=(k_m,0)$ into Eq. (13), the energy functional E of the system is simply a function of the variational parameters R and s, which means that once R and s are determined, the ground state of the system is completely determined.

In Fig. 1, we plot the energy band structure as a function of R and s for different g and g_{12}, and we find that the ground-state phases and the collapse stability of the system can be manipulated by the periodic driving strength χ. When $g<0$ and $g_{12}>0$, as shown in Fig. 1(a1), the minimum of the energy occurs at $s\neq 0$ and $R\to 0$, which represents the system collapse. With the increasing of χ, the collapsed BECs can be manipulated into the stable spin-polarized state ($s\neq 0$) with non-zero momentum [i.e., $k_x=k_m=J_0(\chi)k_0s$, the plane wave phase for $\chi=0.5$ in Fig. 1(a2)] and spin-nonpolarized state ($s=0$) with zero momentum [i.e., $k_x=0$, the zero momentum phase for $\chi=1.0$ in Fig. 1(a3)]. When $g>0$

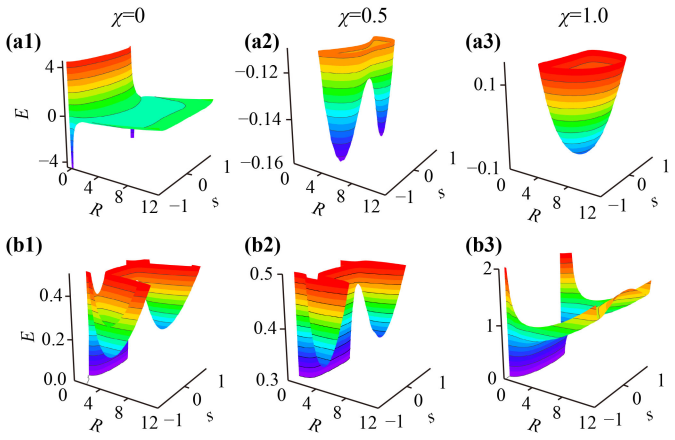

Fig. 1 The energy band of the system as a function of R and s for different g and g_{12}, where $\Omega_0=2.0$ and $\omega=0.1$. **(a1–a3)** for $k_0=1.0$, $g=-15$ and $g_{12}=180$. **(b1–b3)** for $k_0=2.0$, $g=50$ and $g_{12}=-150$.

and $g_{12}<0$, as shown in Fig. 1(b1), the energy possesses two minimum values at $s\neq 0$ and R has a finite value, which means the system is in stable plane wave phase. With the increasing of χ, the system is stable for $\chi=0.5$ [Fig. 1(b2)] and the system collapses for $\chi=1.0$ [Fig. 1(b3)].

Now, the ground state of the system can be determined by minimizing the energy with respect to R and s, i.e., $\partial E/\partial s=0$ and $\partial E/\partial R=0$, and we have

$$\begin{aligned} &s[\frac{(g-g_{12})(1+J_0(2\chi))}{8\pi R^2}+\frac{\Omega_0}{2\sqrt{1-s^2}}-k_0^2J_0^2(\chi)]=0,\\ &\omega^2R-\frac{4\pi+g+g_{12}}{4\pi R^3}-\frac{s^2(g-g_{12})(1+J_0(2\chi))}{8\pi R^3}=0, \end{aligned} \tag{14}$$

then we get

$$\begin{aligned} &R=\left[\frac{4\pi+g+g_{12}}{4\pi\omega^2}+\frac{s^2(g-g_{12})(1+J_0(2\chi))}{8\pi\omega^2}\right]^{1/4},\\ &s=\sqrt{1-\left[2k_0^2J_0^2(\chi)\Omega_0^{-1}-\frac{(g-g_{12})(1+J_0(2\chi))}{4\pi R^2\Omega_0}\right]^{-2}}\\ &\text{or}\quad s=0. \end{aligned} \tag{15}$$

Therefore, the ground state of the system is determined by Eq. (15). According to Eq. (15), the phase transition between the zero momentum phase and the plane wave phase occurs at a critical RC Ω_c with $s=0$, and Ω_c can be written as

$$\Omega_c=2J_0^2(\chi)k_0^2-\frac{\omega(g-g_{12})(1+J_0(2\chi))}{2\sqrt{\pi(4\pi+g+g_{12})}} \tag{16}$$

for $g+g_{12}>-4\pi$. When $\Omega_0<\Omega_c$, the system is in plane wave phase ($s\neq 0$), otherwise, when $\Omega_0>\Omega_c$, the system is in zero momentum phase ($s=0$). The Raman coupling induces the overlap between the two spin states, contributing to the emergence of phase I (spin-nonpolarized phase with zero momentum), while the SO coupling causes spin polarization of the system, which promotes the emergence of phase II (spin-polarized phase with non-zero momentum). The repulsive interspecies interaction or weaker attractive intraspecies interaction with $g_{12}>g$ effectively inhibits the overlap between the two spin states, resulting in spin polarization, while the weaker attractive interspecies interaction with $g_{12}<g$ can promote the emergence of phase I by increasing the overlap of the two spin states. These effects are more enhanced with a stronger harmonic potential and clearly predicted by Eq. (16). Eq. (16) shows that the competition among the RC, effective SO coupling $J_0(\chi)k_0$, effective atomic interaction $\frac{(g-g_{12})[1+J_0(2\chi)]}{\sqrt{4\pi+g+g_{12}}}$ and trapping potential ω determines the ground-state phase transition. The periodic driving $J_0(\chi)$ further modifies the effective SO coupling strength and interatomic interaction of the system (the modification of the atomic interaction is more obvious for the strong harmonic potential), which results in the manipulation of the phase transition of the system by the periodic driving. These will be clearly illustrated in the following discussions.

4 Phase transition

In the above section, by using the variational method, we determined the ground-state phases of the system and obtained the phase transition boundary between the zero momentum phase and the plane wave phase. In this section, we investigate in detail the effect of the periodic driving of RC on the ground-state phases and phase transition boundary of BECs with tunable SO coupling in two-dimensional harmonic trap.

For our purpose, the ground-state phase diagrams of various parameter planes are obtained by the variational method. It is found that the boundary between the plane wave phase and the zero momentum phase can be controlled by varying the periodic driving strength χ. Experimentally, the driving strength χ can be adjusted in real time by adjusting the amplitude Ω_R and frequency ω_R of RC. On the other hand, it is observed that for the strong repulsive and weaker attractive interaction, the phase transition is determined by the coupling between SO coupling, RC, interatomic interaction and external trapping potential.

In Fig. 2, we plot the quasimomentum k_m of the ground-state as a function of the RC Ω_0 for various χ with $g>g_{12}$, $g=g_{12}$ and $g<g_{12}$. It is clear that the system has a spin-polarized phase with non-zero momentum (i.e., plane wave phase, called as phase II) for $\Omega_0<\Omega_c$ and a spin-nonpolarized phase with zero momentum (i.e., zero momentum phase, called as phase I) for $\Omega_0>\Omega_c$. With the increasing of χ, the critical Ω_c decreases gradually, which means the system will undergo a phase transition from the phase II to the phase I when χ increases. Moreover, when the harmonic potential is stronger, the phase transition is more sensitive to the periodic driving strength χ and interatomic interaction. When $g=g_{12}$ [Figs. 2(b1)–(b2)], according to Eq. (16), the phase transition occurs at $\Omega_c=2J_0^2(\chi)k_0^2$, which is consistent with the case of phase transition point of the single particle case in free space. For a fixed periodic driving strength χ, the phase transition point of the system exists in the $\Omega_c<2J_0^2(\chi)k_0^2$ region when there has the weaker attractive interspecies interaction [i.e., $g>g_{12}$, Figs. 2(a1)–(a2)], and the phase transition point appears in the $\Omega_c>2J_0^2(\chi)k_0^2$ region when the system is dominated by strong repulsive interspecies interaction [i.e., $g<g_{12}$, Figs. 2(c1)–(c2)]. In addition, the increasing of harmonic potential frequency ω will promote the appearance of phase I for $g>g_{12}$ and phase II for $g<g_{12}$.

As shown in Fig. 3, in order to investigate the relationship between the periodic driving strength χ and the phase

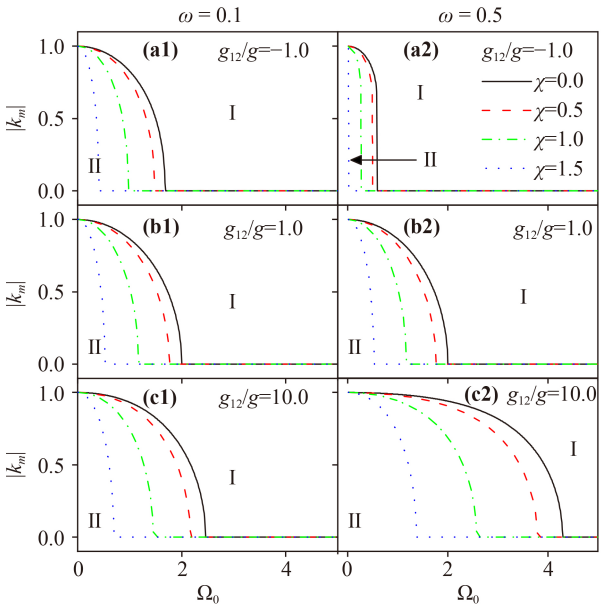

Fig. 2 Quasimomentum k_m corresponding to the minimum of energy as a function of Ω_0 for different g_{12}, ω and χ, where $g = 10$ and $k_0 = 1.0$. $\omega = 0.1$ for the left column and $\omega = 0.5$ for the right column.

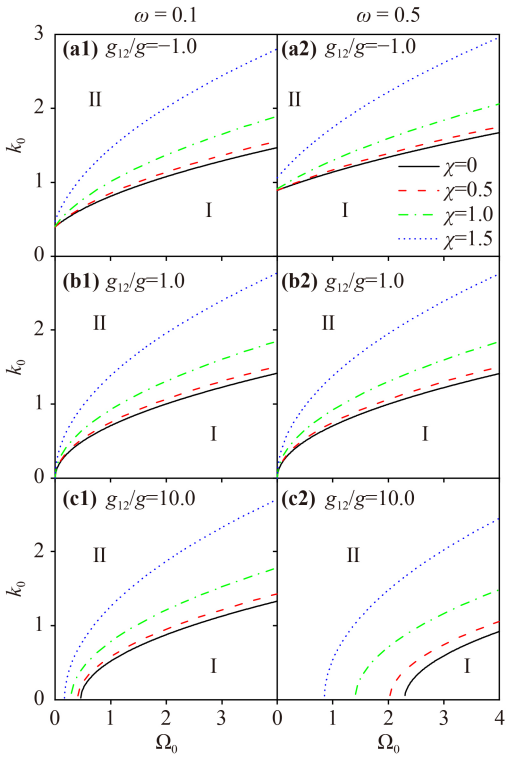

Fig. 3 Phase diagram in Ω_0-k_0 plane for different g_{12}, ω and χ, where $g = 10$. $\omega = 0.1$ for the left column and $\omega = 0.5$ for the right column.

transition, we plot the ground-state phase diagrams in Ω_0-k_0 plane for various χ with $g > g_{12}$, $g = g_{12}$ and $g < g_{12}$. As the RC Ω_0 increases for fixed χ, k_0 and g_{12}/g, the phase transition from phase II to phase I occurs in the system. RC increases the overlap between the two spin states, which contributes to the emergence of phase I. Similarly, for fixed χ, Ω_0 and g_{12}/g, the increasing of SO coupling strength k_0 causes spin polarization of the system, which means phase transition from phase I (spin-nonpolarized phase with zero momentum) to phase II (spin-polarized phase with non-zero momentum) occurs. With the increasing of χ, the region of phase I increases and the region of phase II decreases. This is due to the fact that the increasing of χ decreases the effective SO coupling strength $J_0(\chi)k_0$ and results in the phase transition from phase II to phase I. For a fixed χ, when the interspecies interaction is changed from weak attractive interaction to strong repulsive interaction [Figs. 3(a1), (b1), (c1)], a phase transition from phase I to phase II occurs in the system, which is more obvious for strong harmonic potentials [Figs. 3(a2), (b2), (c2)]. Physically, the repulsive interspecies interaction effectively inhibits the overlap between the two spin states, resulting in spin polarization, which is enhanced in the stronger harmonic potential. Conversely, the weaker attractive interspecies interaction can promote the emergence of phase I by increasing the overlap of the two spin states. In addition, the strong harmonic potential is favorable to the appearance of phase I for $g > g_{12}$ and phase II for $g < g_{12}$, which is well predicted by the phase transition condition Eq. (16).

In order to better understand the effect of the periodic driving strength χ on the phase transition boundary, we plot the critical RC Ω_c and SO coupling strength k_c as a function of χ for different g_{12} with $g = 10$ in Fig. 4 ($k_0 = 1$) and Fig. 5 ($\Omega_0 = 2$), respectively. As shown in Fig. 4, with the increasing of the periodic driving strength χ, the critical Ω_c decreases for weaker attractive interspecies interaction and strong repulsive interspecies interaction. The increasing of χ results in decreasing of the effective SO coupling strength $J_0(\chi)k_0$ that promotes the spin-unpolarization and the appearance of phase I, which means that the ground-state phases of the system can be controlled in real time by changing the intensity and phase of the Raman laser (i.e., the periodic driving strength χ). For fixed χ, the critical Ω_c increases and the system moves from phase I to phase II when the interspecies interaction changes from attractive interaction to repulsive interaction, which is consistent with the conclusion in Fig. (3). According to the phase transition condition Eq. (16), we find that the effect of atomic interaction on the phase boundary can be regulated by the periodic driving strength χ. Furthermore, the influence of the atomic interaction on Ω_c is more obvious when the trapping potential is strong, and the strong harmonic potential leads to the increasing of critical Ω_c for $g < g_{12}$ and the decreasing of critical Ω_c for $g > g_{12}$. At the same time, we plot the average spin polarization of the condensates in phase I and phase II at $g_{12}/g = 1.5$ for Figs. 4(a1)–(a2)

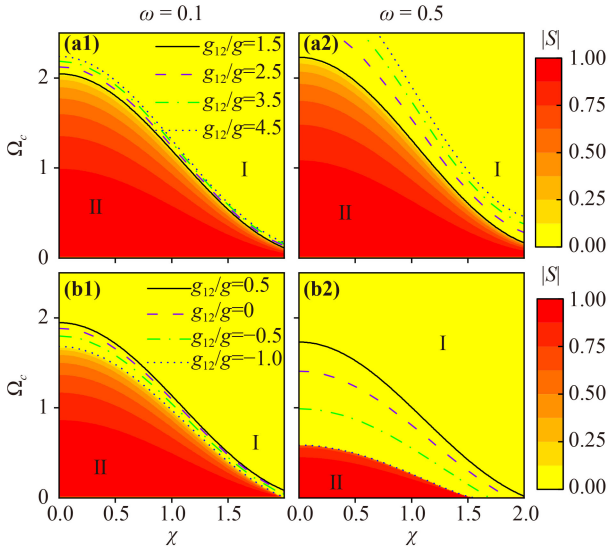

Fig. 4 The critical RC Ω_c as a function of χ, where $g = 10$ and $k_0 = 1$. $\omega = 0.1$ for the left column and $\omega = 0.5$ for the right column.

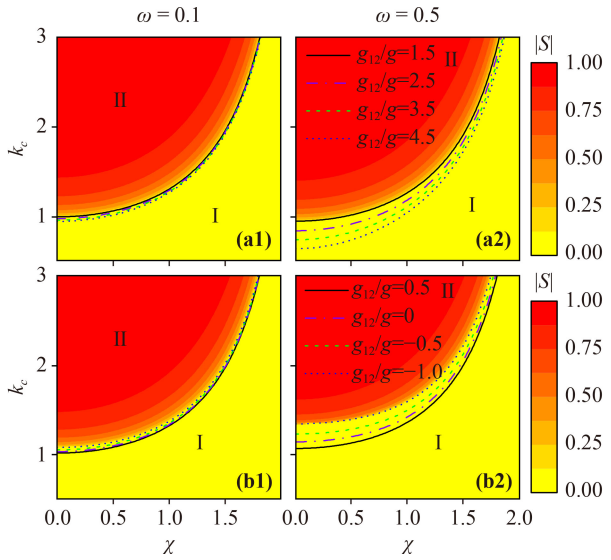

Fig. 5 The critical SO coupling strength k_c as a function of χ, where $g = 10$ and $\Omega_0 = 2.0$. $\omega = 0.1$ for the left column and $\omega = 0.5$ for the right column.

and $g_{12}/g = -1.0$ for Figs. 4(b1)–(b2), respectively. It is clear that phase II is a spin-polarized state with nonzero momentum (i.e., plane wave phase), and phase I is a spin-nonpolarized state with zero momentum (i.e., zero momentum phase). If in the beginning $\Omega_0 < \Omega_c$, the system is in the phase II. Then with the increasing of the periodic driving strength χ, the critical RC Ω decreases, and the system will undergo a phase transition from phase II to phase I at the point $\Omega = \Omega_c$.

As shown in Fig. 5, the phase diagram in the $\chi - k_c$ plane is obtained in a similar way. With the increasing of the periodic driving strength χ, the critical SO coupling strength k_c increases for weaker attractive interspecies interaction and strong repulsive interspecies interaction, which leads to a phase transition from phase I to phase II, so the region of phase I is decreasing and the region of phase II is increasing. When $g < g_{12}$ [Figs. 5(a1)–(a2)], with the increasing of g_{12}, the phase transition boundary moves to a smaller value of critical SO coupling strength k_c for fixed χ, which results in the increasing of the region of phase II and means the strong repulsive interspecies interaction weaken the overlap of the two spin states and is favorable for the appearance of phase II. In this case, the increasing of harmonic potential frequency ω will promote the appearance of phase II, which is especially evident in the case of strong interspecies interaction. When $g > g_{12}$ [Figs. 5(b1)–(b2)], the phase boundary moves towards a larger k_c with the decreasing of g_{12}, which leads to the increasing of the region of phase I. Thus, the weaker attractive intraspecies interaction promotes the emergence of phase I. At this time, the increasing of harmonic potential frequency ω also promotes the appearance of phase I, which is obvious in the case of weaker attractive interspecies interaction. In particular, since the smaller SO coupling strength is favorable for the emergence of phase I, and the effective SO coupling strength $J_0(\chi)k_0$ decreases with the increasing of χ for fixed g_{12}/g and k_0, which leads to the phase transition from phase I to phase II. Similarly, we plot the average spin polarization of the condensates in phase I and phase II at $g_{12}/g = 1.5$ for Figs. 5(a1)–(a2) and $g_{12}/g = -1.0$ for Figs. 5(b1)–(b2), respectively. It is obvious that phase I is zero momentum phase and phase II is plane wave phase.

In a word, according to the phase transition condition Eq. (16), the coupling between SO coupling, RC, interatomic interaction and external trapping potential determines the phase boundary of the system. Interestingly, the interatomic interaction and SO coupling strength can be regulated by the periodic driving strength, so the periodic driving strength can change the phase boundary of the system. Furthermore, it is found that the strong RC can promote the appearance of zero momentum phase (i.e., phase I), the strong SO coupling strength and repulsive interspecies interaction can promote the emergence of plane wave phase (i.e., phase II). Thus, the ground-state phase transition can be manipulated in real time by periodic driving strength, which can be achieved in the current experiment.

5 The collapse stability

In the previous section, we studied the effect of the periodic driving strength χ on the ground-state phases, and we find that the periodic driving of RC can manipulate the ground-state phases by changing the effective SO coupling strength $J_0(\chi)k_0$ and interatomic interaction. In this section, we investigate in detail the manipulation of the collapse stability of the ground-state phases by the periodic driving of RC. First, the analytical prediction of

the stability boundary of the ground-state phases is obtained by the variational method. Then, we plot the stability diagram and illustrate the physical mechanism. Finally, the theoretical analysis is tested by simulating the G–P equation of the system.

5.1 The stability analysis

The eigenvalue of Hessian matrix should be positive for the stable ground-state. Thus R and s, which have been obtained by Eq. (14), must satisfy $\partial^2 E/\partial R^2 > 0$ and $(\partial^2 E/\partial s^2)(\partial^2 E/\partial R^2) - (\partial^2 E/\partial R \partial s)^2 > 0$, one obtains

$$4\omega^2[\frac{(g-g_{12})(1+J_0(2\chi))}{8\pi R^2} + \frac{\Omega_0}{2(1-s^2)^{3/2}} - k_0^2 J_0^2(\chi)] - \frac{[(g-g_{12})(1+J_0(2\chi))s]^2}{16\pi^2 R^6} > 0. \tag{17}$$

Therefore, once R and s are obtained by Eq. (14), the existence of a stable ground-state of the BECs can be tested by Eq. (17). The wave packet width $R \to 0$ means that the system is unstable (i.e., collapse). On the contrary, the width R of the stable ground-state corresponds to a finite value. Moreover, the occurrence of different ground-state of the system depends on the value of s.

When $s = 0$, most atoms condense into the zero momentum state $(k_x, k_y) = (0, 0)$ and are equally distributed between the two spin states, which means that the system is in the zero momentum phase (i.e., phase I). In this case, the minimum point of energy in a band structure diagram appears at $s = 0$ and we can acquire the corresponding wave packet width

$$R = \left(\frac{4\pi + g + g_{12}}{4\pi\omega^2}\right)^{1/4}. \tag{18}$$

By substituting it into Eq. (17), the condition for the existence of stable phase I is obtained. For $\Omega_0 \geq 2J_0^2(\chi)k_0^2$, the condition is given by

$$\begin{aligned} &g + g_{12} > -4\pi, \\ &g - g_{12} > f_{\rm zm}. \end{aligned} \tag{19}$$

For $\Omega_0 < 2J_0^2(\chi)k_0^2$, the condition is written as

$$\begin{aligned} &g + g_{12} > -4\pi, \\ &g + g_{12} < -4\pi + f_{\rm pw} \\ &\qquad \text{when } g_{12}^c - g^c \leq g_{12} - g \leq 0, \\ &g - g_{12} > f_{\rm zm} \\ &\qquad \text{when } g_{12} - g < g_{12}^c - g^c, \end{aligned} \tag{20}$$

where

$$f_{\rm zm} = [2J_0^2(\chi)k_0^2 - \Omega_0] \cdot \frac{2\sqrt{\pi(4\pi + g + g_{12})}}{\omega[1 + J_0(2\chi)]}, \tag{21}$$

$$f_{\rm pw} = \frac{1}{2}(g-g_{12})[1+J_0(2\chi)] \cdot \{[((g-g_{12})(1+J_0(2\chi)))^{1/3} + (2\pi\omega^{-2}\Omega_0^2)^{1/3}]^3/[8\pi J_0^4(\chi)k_0^4] - 1\}, \tag{22}$$

and (g_{12}^c, g^c) is the intersected point of $g - g_{12} = f_{\rm zm}$ and $g + g_{12} = -4\pi + f_{\rm pw}$.

When $s \neq 0$, most atoms condense into the $(k_x, k_y) = (\pm k_m, 0)$ state and the different distributions of atoms in the two spin states depend on the value of s, which means the system is in the plane wave phase (i.e., phase II). In this case, the energy of the system has two minimum points at $s \neq 0$, and Eq. (17) can be written as

$$\frac{(1-s^2)^{3/2}}{R^6} < \frac{32\pi^2\omega^2\Omega_0}{[(g-g_{12})(1+J_0(2\chi))]^2}. \tag{23}$$

By inserting it into Eq. (14), the condition for existing stable phase II is

$$\begin{aligned} &[3 + J_0(2\chi)]g + [1 - J_0(2\chi)]g_{12} > -8\pi \\ &\qquad \text{when } g_{12} - g > \frac{2\pi\omega^{-2}\Omega_0^2}{1 + J_0(2\chi)}, \\ &g + g_{12} > -4\pi + f_{\rm pw} \\ &\qquad \text{when } g_{12}^c - g^c \leq g_{12} - g \leq \frac{2\pi\omega^{-2}\Omega_0^2}{1 + J_0(2\chi)}, \\ &g - g_{12} < f_{\rm zm} \\ &\qquad \text{when } g_{12} - g < g_{12}^c - g^c. \end{aligned} \tag{24}$$

The above equations show that the system is in the stable phase I when Eqs. (19) and (20) are satisfied, and the system is in the stable phase II when Eq. (24) is satisfied. However, outside these regions means that the system collapses. The controllable stability conditions Eqs. (19)–(24) of these ground-state phases are our main results.

5.2 The stability phase diagram

The stability diagram in $g-g_{12}$ plane with different periodic driving strength χ and SO coupling strength k_0 is shown in Fig. 6. Obviously, the $g-g_{12}$ plane is divided into the unstable collapse region and the stable ground-state phases region (i.e., the stable phase I and II), which strongly depends on $\Omega_0/[2J_0^2(\chi)k_0^2]$. Furthermore, for BECs without RC and SO coupling (i.e., $\Omega_0 = k_0 = \chi = 0$), the collapse occurs at $g < -2\pi$ for $g_{12} > -2\pi$ or $g + g_{12} < -4\pi$ for $g_{12} < -2\pi$, which is in good accordance with the collapse boundary predicted by previous theory [11], and observed in the experiments [11, 12, 51]. Thus, our theoretical methods and relevant conclusions are reasonable. Moreover, the collapse can be stabilized with χ when k_0 and Ω_0 are fixed to a constant, and the stabilizing mechanisms are described quantitatively as follows.

When $\Omega_0 \geq 2J_0^2(\chi)k_0^2$ [Figs. 6(a1)–(a4)], compared to the case of $\chi = 0$ [Fig. 6(a1)], as the increasing of χ for the fixed value of Ω_0 and k_0 [Figs. 6(a2)–(a4)], the phase

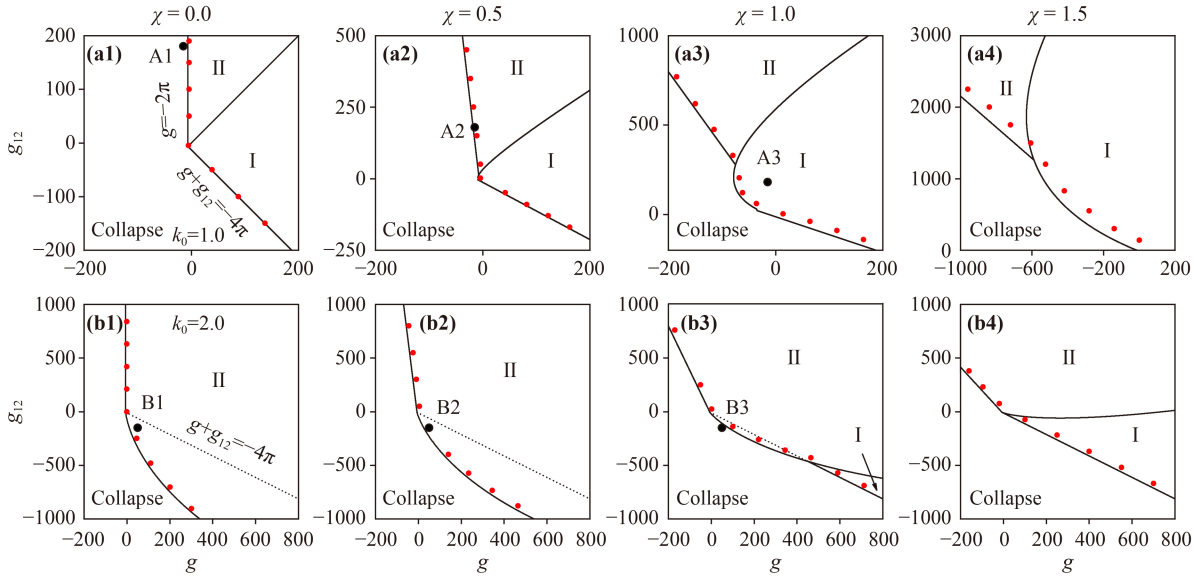

Fig. 6 Stability diagram in $g-g_{12}$ plane with different SO coupling strength ($k_0 = 1.0$ for the top row, where $\Omega_0 \geq 2J_0^2(\chi)k_0^2$; $k_0 = 2.0$ for the bottom row, where $\Omega_0 < 2J_0^2(\chi)k_0^2$.) and χ for ω=0.1, $\Omega_0 = 2.0$ and $\omega_R = 20$. The border of regions is obtained by using the variational calculation (the black solid line) and the complete numerical simulation of the G–P equation acquired from the Hamiltonian Eq. (1) (red dots). A1–A3 and B1–B3 are selected points corresponding to **(a1)**–**(a3)** and **(b1)**–**(b3)** in Fig. 1.

transition boundary between phase I and phase II is expanded to the strong repulsive interspecies interaction region (i.e., lager positive g_{12}). The increasing of χ leads to the phase transition from phase II to phase I, which is consistent with the conclusion obtained in Section 4. On the other hand, with the increasing of χ, the boundaries between the collapse region and the stable region (i.e., phase I and phase II) are expanded into the region of strong attractive intraspecies interaction (i.e., $g < -2\pi$, where the collapse occurs when $\chi = 0$), which means that the collapse caused by attractive intraspecies interaction is gradually stabilized by the increasing of χ, and the physical mechanism of stability is shown below. In energy functional Eq. (13), the periodic driving strength can manipulate the SO coupled energy term and spin-dependent interaction term of the system, which leads to the manipulation of the energy band structure of the ground state and the occurrence of stable minimum points in the band structure, thus the system can be stabilized. In fact, when $\chi < 4$, the value of zero-order Bessel function $J_0(\chi)$ decreases as χ increases, and the ratio $\Omega_0/[2J_0^2(\chi)k_0^2]$ increases as χ increases when $\Omega_0/[2J_0^2(\chi)k_0^2] > 1$. It is reasonable to think that the consequence of decreasing of $J_0(\chi)$ is that the effective SO coupling strength $J_0(\chi)k_0$ will be reduced; thus, the value of RC is larger compared to SO coupling strength. Qualitatively, the overlap between the two pseudo-spin states is enhanced by RC, which can inhibit the collapse induced by attractive intraspecies interaction, but the collapse caused by attractive interspecies interaction is not affected by RC. The quantitative mechanism for manipulating of collapse can be derived by Eq. (19), and the critical condition for existing stable phase I is given by

$$g_c = -2\pi + \frac{1}{2}f_{\rm zm}. \tag{25}$$

It is clear that $f_{\rm zm} \leq 0$ for $\Omega_0 \geq 2J_0^2(\chi)k_0^2$ and $f_{\rm zm}$ decreases as χ increases [see Eq. (21)]. Therefore, with the increasing of χ, $g_c < -2\pi$ decreases, the stable phase I will expand into the region of strong attractive interspecies interaction. On the other hand, according to Eq. (24), the boundary of phase II and collapse can be written as

$$g_c = \frac{J_0(2\chi) - 1}{3 + J_0(2\chi)}g_{12} - \frac{8\pi}{3 + J_0(2\chi)} \tag{26}$$

for $g_{12} - g > 2\pi\omega^{-2}\Omega_0^2/[1 + J_0(2\chi)]$. The slope of g_c against g_{12} is $[J_0(2\chi) - 1]/[3 + J_0(2\chi)]$, which is always negative and decreases as χ increases, which results in $g_c < 0$ decreasing with χ. Hence, the boundary between phase II and collapse region moves to the region of strong attractive intraspecies interaction. Eqs. (25) and (26) show that, SO coupling and RC result in an effective repulsive interspecies interaction, while the periodic driving of RC enhanced this effective repulsive interspecies interaction, which compensates for the attractive intraspecies interaction.

When $\Omega_0 < 2J_0^2(\chi)k_0^2$ [Figs. 6(b1)–(b4)], with the increasing of χ, the stable phase II region also moves to the stronger attractive intraspecies interaction region [Figs. 6(b2)–(b4)], where the BECs are unstable for $\chi = 0$ [Fig. 6(b1)], which is easily understand by Eq. (24). The periodic driving of RC produces the effective repulsive interspecies interaction (i.e., $[1 - J_0(2\chi)]g_{12}$) that prevents

the collapse of the system and can be manipulated by the periodic driving. Meanwhile, as χ increases, a phase transition from phase II to phase I occurs, which results in the increasing of the stable phase I region, and its physical mechanism is consistent with the case of $\Omega_0 \geq 2J_0^2(\chi)k_0^2$. On the other hand, when $\Omega_0 < 2J_0^2(\chi)k_0^2$, the stable phase II region appears below the critical boundary $g + g_{12} = -4\pi$ for the smaller χ [Figs. 6(b1)–(b3)], where the BECs collapse due to strong attractive interspecies interactions for $\Omega_0 > 2J_0^2(\chi)k_0^2$ [Figs. 6(a1)–(a3)]. Detailed physical mechanisms are discussed below. Qualitatively, when $\Omega_0/[2J_0^2(\chi)k_0^2] < 1$, the spin-polarized ground state with a large s can prevent the collapse induced by strong attractive interspecies interaction, but it cannot stabilize the collapse caused by attractive intraspecies interaction. However, as the increasing of χ [Figs. 6(b1)–(b4)], the stable phase II region below the critical boundary $g + g_{12} = -4\pi$ gradually decreases until it disappears. According to Eq. (24), the boundary between the stable phase II region below the critical line $g + g_{12} = -4\pi$ and collapse region can be written as

$$f_{\rm pw} = g + g_{12} + 4\pi. \tag{27}$$

According to Eq. (22), when $g > 0$ and $g_{12} < 0$, $f_{\rm pw}$ is positive and increases as χ increases. Thus, with the increasing of χ, the value of g and g_{12} will be increased, which means the region of stable phase II disappears in the region of strong attractive interspecies interaction. On the other hand, when $\Omega_0 < 2J_0^2(\chi)k_0^2$, strong SO coupling can stabilize the collapse induced by the attractive interspecies interaction; but, the effective SO coupling strength $J_0(\chi)k_0$ decreases as χ increases, which makes the stabilized BECs tend to collapse.

As shown in Fig. 7, in order to further understand the relationship between periodic driving strength χ and stability, we plot the stability diagram in $\chi - k_0$ plane with different interatomic interaction and Ω_0. In the case of collapse induced by attractive intraspecies interaction [Figs. 7(a1)–(a2)], when $\Omega_0 \geq 2J_0^2(\chi)k_0^2$, with the increasing of χ, the collapsed BECs is stabilized into the stable phase II and finally into the stable phase I. On the other hand, the region of collapse caused by attractive intraspecies interaction decreases as Ω_0 increases, which means this collapse can be stabilized by strong RC, and the collapse can be stabilized by a smaller χ for the fixed k_0 and strong RC. In the case of collapse induced by attractive interspecies interaction [Figs. 7(b1)–(b2)], when $\Omega_0 < 2J_0^2(\chi)k_0^2$, with the increasing of χ, the stable phase II collapses due to attractive interspecies interaction. At the same time, with the increasing of Ω_0, the region of stable phase II decreases and the collapse induced by attractive interspecies interaction occurs at a smaller χ for the fixed k_0. In addition, in these two cases, the strong harmonic potential results in the collapse region is increasing and the stable phase I or phase II region is decreasing.

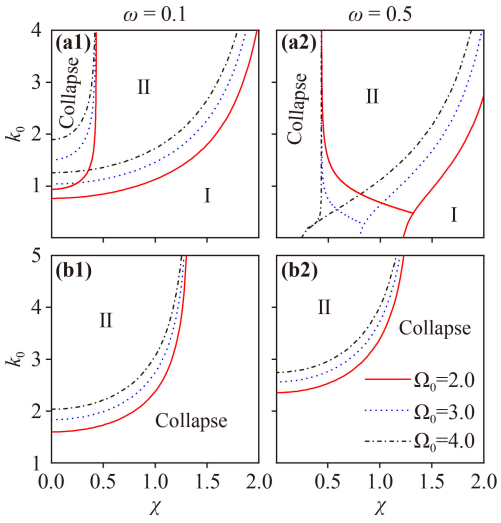

Fig. 7 Stability diagram in χ–k_0 plane with different interatomic interactions. Here $\omega = 0.1$ for the left column and $\omega = 0.5$ for the right column, and the top row for $g = -15$, $g_{12} = 180$ and the bottom row for $g = 50$, $g_{12} = -150$.

When the harmonic potential is ignored (i.e., the trapping frequency $\omega = 0$), the ground state energy functional Eq. (13) with Eq. (14) satisfies $\partial^2 E/\partial R^2 \equiv 0$. That is, the stability condition $\partial^2 E/\partial R^2 > 0$ is not satisfied, a stable self-bound state in free space cannot be formed. However, as discussed in Refs. [52–54], in the one-dimensional spin–orbit-coupled system with Lee–Huang–Yang correction, a self-bound supersolid stripe phase and a zero-minimum droplet state in free space can exist.

6 The collapse dynamics

In the previous section, we have studied the ground-state phase transition and collapse stability of BECs with tunable SO coupling in the harmonic potential. Now we investigate how does the periodic driving of RC affect the collapse dynamic properties of the system, to be specific, the effect of the periodic driving strength χ on the collapse time and collapse velocity is studied. In addition, the variational approximation is confirmed by numerical simulation of G–P equation.

6.1 The variational analysis

In order to investigate the collapse dynamics by variational method, we apply the following Gaussian trial wave function

$$\begin{pmatrix} \psi_1 \\ \psi_2 \end{pmatrix} = \frac{1}{\sqrt{2\pi}R} \cdot \begin{pmatrix} \mathrm{e}^{\frac{\mathrm{i}\phi}{2}}\sqrt{1+s} \\ -\mathrm{e}^{-\frac{\mathrm{i}\phi}{2}}\sqrt{1-s} \end{pmatrix} \times \exp\left(-\frac{\boldsymbol{r}^2}{2R^2} + \mathrm{i}\boldsymbol{k}\cdot\boldsymbol{r} + \frac{\mathrm{i}\beta}{2}\boldsymbol{r}^2\right), \tag{28}$$

with the variational rate of the wave packet width β and the phase difference between the two pseudo-spin states ϕ. Upon substituting the trial wave function into the Lagrangian $\pounds = \int[(\mathrm{i}/2)(\Phi^*\dot{\Phi} - \dot{\Phi}^*\Phi) - \Phi^*(\bar{H}_0 + \bar{H}_{int})\Phi]\mathrm{d}\boldsymbol{r}$, one can obtain:

$$\pounds = -\frac{1}{2}R^2\dot{\beta} - \frac{1}{2}s\dot{\phi} - E, \tag{29}$$

$$\begin{aligned} E =& \frac{1}{2}(k_x^2 + k_y^2 + k_0^2 + \omega^2 R^2 + R^2\beta^2) - J_0(\chi)k_0k_x s \\ &+ \frac{1}{2R^2} + \frac{g + g_{12}}{8\pi R^2} + \frac{s^2(g - g_{12})[1 + J_0(2\chi)]}{16\pi R^2} \\ &- \frac{\Omega_0}{2}\sqrt{1 - s^2}\cos\phi, \end{aligned} \tag{30}$$

where E represents the mean-field energy functional of the system.

Applying the Euler–Lagrangian equations $\partial\pounds/\partial q_i - \mathrm{d}(\partial\pounds/\partial\dot{q}_i)/\mathrm{d}t = 0$, where the variational parameters $q_i = \{k_x, k_y, R, \beta, s, \phi\}$, and we can obtain:

$$(k_x, k_y) = (J_0(\chi)k_0 s, 0), \tag{31}$$

$$\dot{s} = \Omega_0\sqrt{1 - s^2}\sin\phi, \tag{32}$$

$$\dot{\phi} = s\left[2k_0^2J_0^2(\chi) - \frac{(2 + 6J_0(2\chi))(g - g_{12})}{16\pi R^2} + \frac{\Omega_0\cos\phi}{\sqrt{1 - s^2}}\right], \tag{33}$$

$$\begin{aligned} \ddot{R} =& R^{-3} - \omega^2 R + \frac{\{3 + J_0(2\chi) - [1 + 3J_0(2\chi)]s^2\}g_{12}}{16\pi R^3} \\ &+ \frac{\{5 - J_0(2\chi) + [1 + 3J_0(2\chi)]s^2\}g}{16\pi R^3}. \end{aligned} \tag{34}$$

Eqs. (32)–(33) represent the spin dynamics of the system, while the breathing behavior of the BECs can be described by Eq. (34). Obviously, the spin dynamics and breathing dynamics are strongly coupled, which depends on SO coupling, RC and interatomic interaction, and can be adjusted by the periodic driving of RC. The collapse dynamics of the BECs can be controlled by manipulating the effective SO coupling strength $J_0(\chi)k_0$ and interatomic interaction through the periodic driving of RC. When the wave packet width decreases to zero in a limited time, the collapse occurs and the BECs are unstable, otherwise, the BECs are stable in phase I or phase II.

The collapse dynamic of the BECs is demonstrated in Fig. 8, which describes the evolution of wave packet width R over time t under different harmonic potential frequency ω and the periodic driving strength χ, where the SO coupling strength is fixed. For the case of attractive intraspecies interaction and $\Omega_0 > 2J_0^2(\chi)k_0^2$ [Figs. 8(a1)–(a2)], when $\chi < \chi_c$, the wave packet width decreases to zero for a limited time, thus the BECs are unstable and

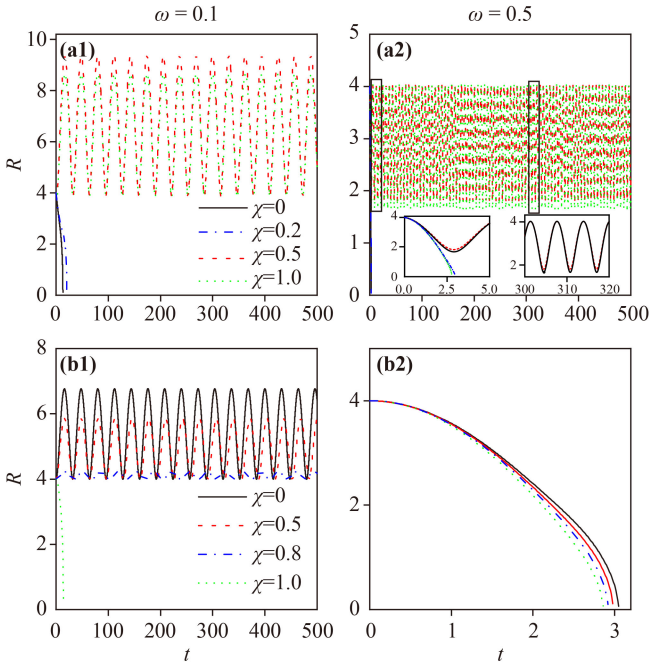

Fig. 8 The time evolution of the wave packet width for different χ with the fixed $\Omega_0 = 2.0$. **(a1, a2)** for $k_0 = 1.0$, $g = -15$ and $g_{12} = 180$, $\chi = 0, 0.5, 1.0$ corresponding to A1–A3 as marked in Fig. 6, respectively. **(b1, b2)** for $k_0 = 2.0$, $g = 50$ and $g_{12} = -150$, $\chi = 0, 0.5, 1.0$ corresponding to B1–B3 as marked in Fig. 6, respectively. Here the left column for $\omega = 0.1$ and the right column for $\omega = 0.5$.

the collapse occurs, where χ_c represents the critical value of periodic driving strength between collapse and stable ground-state [See Fig. 9]. When $\chi \geq \chi_c$, the wave packet width always oscillates near the equilibrium state, thus the BECs are stable and the system enters the stable phase I or phase II. With the increasing of χ, the collapse time is prolonged and the collapse speed is reduced, i.e., the collapsed BECs will be stabilized as χ increases. Moreover, when χ increases to the critical value χ_c, the collapse time is significantly prolonged and the BECs are stable. The lines with $\chi = 0, 0.5$, and 1.0 respectively correspond to the points as marked by A1, A2 and A3 in Fig. 6, which show that the dynamics shown in Fig. 8(a1) agree with the ground state stability shown in Fig. 6. On the other hand, for the case of attractive interspecies interaction and $\Omega_0 < 2J_0^2(\chi)k_0^2$ [Figs. 8(b1)–(b2)], when $\chi < \chi_c$, the wave packet width R is a finite value and the BECs are always stable; when $\chi > \chi_c$, the wave packet width decreases to zero in a finite time, and the BECs collapse. With the increasing of χ, the collapse time is shortened and the collapse speed is accelerated, i.e., the stable BECs collapses gradually as χ increases. As χ increases to the critical value χ_c, the stable condensates begins to collapse. The lines with $\chi = 0, 0.5$, and 1.0 respectively correspond to the points as marked by B1, B2 and B3 in Fig. 6, which show that the dynamics shown in Fig. 8(b1) agree with

the ground state stability shown in Fig. 6. In addition, for both attractive intraspecies and interspecies interactions, the strong harmonic potential decreases the collapse time and accelerates the collapse speed. Thus, in the experiment, the collapse time and collapse speed of the BECs can be controlled by the periodic driving strength χ.

Figure 9 describes how the collapse threshold χ_c is affected by the SO coupling strength k_0, RC constant Ω_0 and harmonic potential, i.e., the trapping frequency of transverse plane ω. For attractive intraspecies interaction, with the increasing of RC constant Ω_0 [Fig. 9(a1)] or the decreasing of SO coupling strength k_0 [Fig. 9(a2)], the collapse time is prolonged and the collapse velocity is reduced, and with a smaller critical χ_c can stabilize the collapsed BECs and make it enter phase I. On the other hand, for attractive interspecies interaction, the critical χ_c decreases with the increasing of RC constant Ω_0 [Fig. 9(b1)] and χ_c increases with the increasing of SO coupling strength k_0 [Fig. 9(b2)]; thus the strong SO coupling strength k_0 transforms the collapsed BECs into the stable phase II; meanwhile, the collapse time is gradually shortened and the collapse speed is accelerated as the decreasing of k_0 or the increasing of Ω_0. In addition, as the increasing of ω, the critical value χ_c increases for attractive intraspecies interaction case [Fig. 9(a3)] and χ_c decreases for attractive interspecies interaction [Fig. 9(b3)]. In both cases, the increasing of ω shorten the collapse time gradually, which leads to the larger collapse speed, i.e., the collapse more easily takes place.

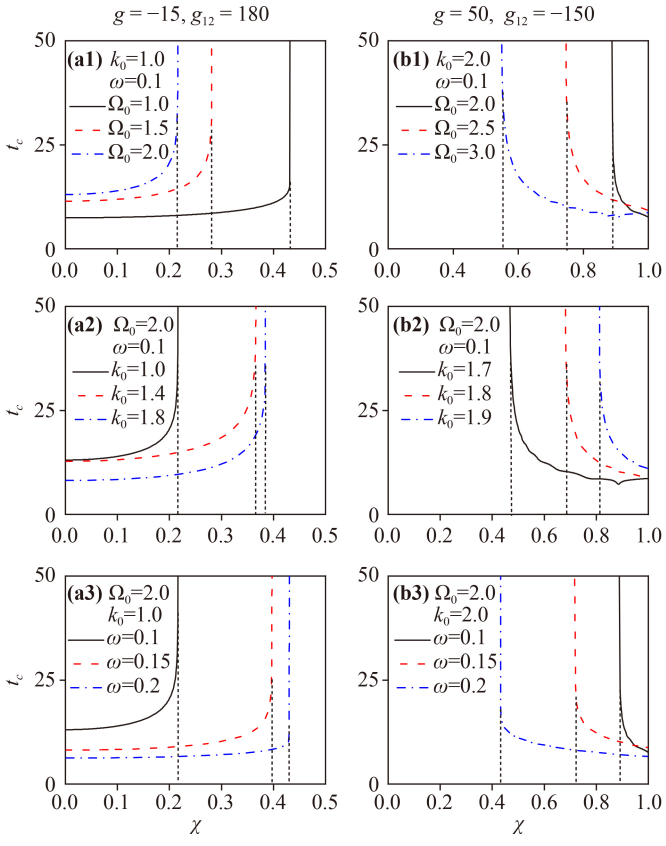

Fig. 9 The critical collapse time t_c versus χ for different phases by means of the variational method. The vertical black dot lines represent the values of χ_c. Here the left column for $g = -15$, $g_{12} = 180$ and the right column for $g = 50$, $g_{12} = -150$.

In short, our analysis provides a theoretical guidance for real-time manipulation of the collapse dynamics in the experiments.

6.2 The numerical simulation

In order to confirm the variational approximation, the fourth-order Runge–Kutta method is used for numerical simulation of the original G–P equation, i.e., Eqs. (1)–(4). In the simulation, the modulation frequency of periodic driving of RC $\omega_R = 20$ is fixed; thus the periodic driving strength of RC $\chi = 0, 0.5, 1.0$ correspond to the modulation amplitude $\Omega_R = 0, 10, 20$, respectively. As shown in Fig. 10, we plot the dynamical evolution of the wave packets. Figs. 10(a1)–(a3) correspond to the points as marked by A1–A3 in Figs. 6(a1)–(a3), respectively; and Figs. 10(b1)–(b3) correspond to the points as marked by B1–B3 in Figs. 6(b1)–(b3), respectively. When $\Omega_0 \geq 2J_0^2(\chi)k_0^2$ [Figs. 10(a1)–(a3)], with the increasing of χ, the collapse [Fig. 10(a1)] caused by attractive intraspecies interaction is stabilized, and then the system enters the stable phase II [Fig. 10(a2)] and phase I [Fig. 10(a3)], which are consistent with Figs. 6(a1)–(a3) and Fig. 7(a1). When $\Omega_0 < 2J_0^2(\chi)k_0^2$ [Figs. 10(b1)–(b3)], with the increasing of χ, the stable phase II [Figs. 10(b1)–(b2)] collapses [Fig. 6(b3)] due to the attractive interspecies interaction, which is consistent with Figs. 6(b1)–(b3) and Fig. 7(b1). Meanwhile, Fig. 10 is consistent with the corresponding band structure in Fig. 1. In addition, the numerical results of the boundary between the collapsed region and the stable region are represented by red dots in Fig. 6, which is in good agreement with the variational predicted boundary. Thus, theoretical predictions are confirmed by these numerical results.

7 Conclusions

In conclusion, in two-dimensional harmonic potential, by using the variational method and numerical simulation, we have studied the phase transition, stability phase diagrams and collapse dynamics of the BECs with tunable SO coupling and the periodic driving of RC. The effective time-independent Floquet Hamiltonian of the BECs with tunable SO coupling and two-body interactions is obtained by using the high frequency approximation in the external potential. And then, the Gaussian wave function is selected to predict the analytical conditions of the phase transition boundary and the stability diagram of the BECs with tunable SO coupling by using

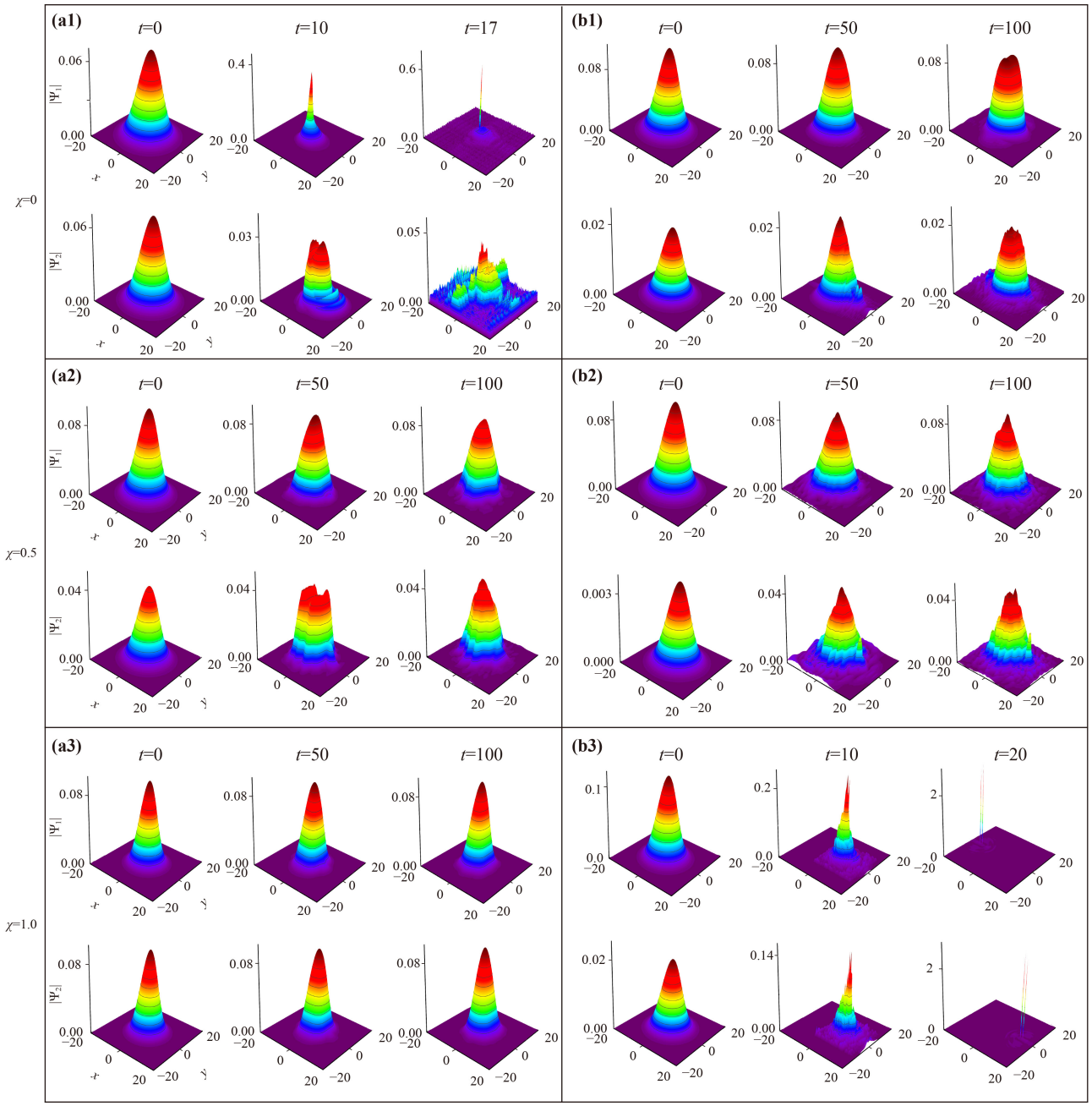

Fig. 10 **(a1–a3)** Dynamical evolution of the wave packets corresponding to the cases as marked by A1, A2 and A3 in Figs. 6(a1)–(a3). **(b1–b3)** Dynamical evolution of the wave packets corresponding to the cases as marked by B1, B2 and B3 in Fig. 6(b1)–(b3).

the variational method. We find that the boundary between spin-nonpolarized phase with zero momentum (phase I) and spin-polarized phase with non-zero momentum (phase II) can be controlled by varying the periodic driving strength, which is more sensitive to strong external trapping. Most importantly, in the BECs with tunable SO coupling and external trapping potential, the stability phase diagram is obtained by the variational method, and the mechanism of collapse stability manipulated by periodic driving of RC is clearly revealed. Furthermore, the collapse dynamics of the BECs with tunable SO coupling can be controlled by the periodic driving strength, which also depends on the RC, SO coupling strength and external trapping potential. Finally, the variational approximation is confirmed by numerical simulation of G–P equation. Notably, our results provide theoretical guidance for manipulating the ground-state stability and collapse dynamics of the SO coupled BECs in real experiments.

Acknowledgements This work was supported by the National Natural Science Foundation of China under Grant Nos. 12164042,

11764039, 11475027, 11865014, 12104374, 11964008, and 11847304; the Natural Science Foundation of Gansu Province under Grant Nos. 17JR5RA076, 20JR5RA194, and 20JR5RA526; the Scientific Research Project of Gansu Higher Education under Grant No. 2016A-005; the Innovation Capability Enhancement Project of Gansu Higher Education under Grant Nos. 2020A-146 and 2019A-014; the Creation of Science and Technology of Northwest Normal University under Grant No. NWNU-LKQN-18-33.

References

1. M. H. Anderson, J. R. Ensher, M. R. Matthews, C. E. Wieman, and E. A. Cornell, Observation of Bose–Einstein condensation in a dilute atomic vapor, *Science* 269(5221), 198 (1995)
2. K. B. Davis, M. O. Mewes, M. R. Andrews, N. J. van Druten, D. S. Durfee, D. M. Kurn, and W. Ketterle, Bose–Einstein condensation in a gas of sodium atoms, *Phys. Rev. Lett.* 75(22), 3969 (1995)
3. R. Rajan, P. R. Babu, and K. Senthilnathan, Photon condensation: A new paradigm for Bose–Einstein condensation, *Front. Phys.* 11(5), 110502 (2016)
4. B. DeMarco and D. S. Jin, Onset of Fermi degeneracy in a trapped atomic gas, *Science* 285(5434), 1703 (1999)
5. P. J. Wang and J. Zhang, Spin-orbit coupling in Bose–Einstein condensate and degenerate Fermi gases, *Front. Phys.* 9(5), 598 (2014)
6. P. Hauke, F. M. Cucchietti, L. Tagliacozzo, I. Deutsch, and M. Lewenstein, Can one trust quantum simulators, *Rep. Prog. Phys.* 75(8), 082401 (2012)
7. M. Ueda and A. J. Leggett, Macroscopic quantum tunneling of a Bose–Einstein condensate with attractive interaction, *Phys. Rev. Lett.* 80(8), 1576 (1998)
8. H. Saito and M. Ueda, Dynamically stabilized bright solitons in a two-dimensional Bose–Einstein condensate, *Phys. Rev. Lett.* 90(4), 040403 (2003)
9. P. Pedri and L. Santos, Two-dimensional bright solitons in dipolar Bose–Einstein condensates, *Phys. Rev. Lett.* 95(20), 200404 (2005)
10. G. D. Montesinos, V. M. Perez-Garćia, and H. Michinel, Stabilized two-dimensional vector solitons, *Phys. Rev. Lett.* 92(13), 133901 (2004)
11. F. Dalfovo, S. Giorgini, L. P. Pitaevskii, and S. Stringari, Theory of Bose–Einstein condensation in trapped gases, *Rev. Mod. Phys.* 71(3), 463 (1999)
12. T. Koch, T. Lahaye, J. Metz, B. Fröhlich, A. Griesmaier, and T. Pfau, Stabilization of a purely dipolar quantum gas against collapse, *Nat. Phys.* 4(3), 218 (2008)
13. C. Chin, R. Grimm, P. Julienne, and E. Tiesinga, Feshbach resonances in ultracold gases, *Rev. Mod. Phys.* 82(2), 1225 (2010)
14. P. G. Kevrekidis, G. Theocharis, D. J. Frantzeskakis, and B. A. Malomed, Feshbach resonance management for Bose–Einstein condensates, *Phys. Rev. Lett.* 90(23), 230401 (2003)
15. R. Horchani, Laser cooling of internal degrees of freedom of molecules, *Front. Phys.* 11(4), 113301 (2016)
16. F. Kh. Abdullaev, J. G. Caputo, R. A. Kraenkel, and B. A. Malomed, Controlling collapse in Bose–Einstein condensates by temporal modulation of the scattering length, *Phys. Rev. A* 67(1), 013605 (2003)
17. S. L. Cornish, N. R. Claussen, J. L. Roberts, E. A. Cornell, and C. E. Wieman, Stable ^{85}Rb Bose–Einstein condensates with widely tunable interactions, *Phys. Rev. Lett.* 85(9), 1795 (2000)
18. S. Sabari and B. Dey, Stabilization of trapless dipolar Bose–Einstein condensates by temporal modulation of the contact interaction, *Phys. Rev. E* 98(4), 042203 (2018)
19. P. M. Lushnikov, Collapse of Bose–Einstein condensates with dipde–dipole interactions, *Phys. Rev. A* 051601(R) (2002)
20. Y. J. Lin, R. L. Compton, K. Jiménez-García, J. V. Porto, and I. B. Spielman, Synthetic magnetic fields for ultracold neutral atoms, *Nature* 462(7273), 628 (2009)
21. Y. J. Lin, R. L. Compton, K. Jimnez-Garca, W. D. Phillip, J. V. Porto, and I. B. Spielman, A synthetic electric force acting on neutral atoms, *Nat. Phys.* 7(7), 531 (2011)
22. Y. J. Lin, K. Jiménez-García, and I. B. Spielman, Spin–orbit-coupled Bose–Einstein condensates, *Nature* 471(7336), 83 (2011)
23. P. Wang, Z. Q. Yu, Z. Fu, J. Miao, L. Huang, S. Chai, H. Zhai, and J. Zhang, Spin–orbit coupled degenerate Fermi gases, *Phys. Rev. Lett.* 109(9), 095301 (2012)
24. Z. Wu, L. Zhang, W. Sun, X. T. Xu, B. Z. Wang, S. C. Ji, Y. Deng, S. Chen, X. J. Liu, and J. W. Pan, Realization of two-dimensional spin–orbit coupling for Bose–Einstein condensates, *Science* 354(6308), 83 (2016)
25. L. Huang, Z. Meng, P. Wang, P. Peng, S. L. Zhang, L. Chen, D. Li, Q. Zhou, and J. Zhang, Experimental realization of two-dimensional synthetic spin–orbit coupling in ultracold Fermi gases, *Nat. Phys.* 12(6), 540 (2016)
26. D. Zhang, T. Gao, P. Zou, L. Kong, R. Li, X. Shen, X. L. Chen, S. G. Peng, M. Zhan, H. Pu, and K. Jiang, Ground-state phase diagram of a spin–orbital–angular–momentum coupled Bose–Einstein condensate, *Phys. Rev. Lett.* 122(11), 110402 (2019)
27. W. Han, G. Juzeliūnas, W. Zhang, and W. M. Liu, Supersolid with nontrivial topological spin textures in spin–orbit-coupled Bose gases, *Phys. Rev. A* 91(1), 013607 (2015)
28. Y. Zhang, M. E. Mossman, T. Busch, P. Engels, and C. Zhang, Properties of spin–orbit-coupled Bose–Einstein condensates, *Front. Phys.* 11(3), 118103 (2016)
29. S. W. Song, L. Wen, C. F. Liu, S. C. Gou, and W. M. Liu, Ground states, solitons and spin textures in spin-1 Bose–Einstein condensates, *Front. Phys.* 8(3), 302 (2013)
30. Y. K. Liu, H. X. Yue, L. L. Xu, and S. J. Yang, Vortex-pair states in spin–orbit-coupled Bose–Einstein condensates with coherent coupling, *Front. Phys.* 13(5), 130316 (2018)
31. H. Sakaguchi, B. Li, and B. A. Malomed, Creation of two-dimensional composite solitons in spin–orbit-coupled self-attractive Bose–Einstein condensates in free space, *Phys. Rev. E* 89(3), 032920 (2014)
32. Y. C. Zhang, Z. W. Zhou, B. A. Malomed, and H. Pu,

Stable solitons in three dimensional free space without the ground state: self-trapped Bose–Einstein condensates with spin–orbit coupling, *Phys. Rev. Lett.* 115(25), 253902 (2015)
33. V. Achilleos, D. J. Frantzeskakis, P. G. Kevrekidis, and D. E. Pelinovsky, Matter-wave bright solitons in spin–orbit coupled Bose–Einstein condensates, *Phys. Rev. Lett.* 110(26), 264101 (2013)
34. S. Mardonov, E. Ya. Sherman, J. G. Muga, H. W. Wang, Y. Ban, and X. Chen, Collapse of spin–orbit-coupled Bose–Einstein condensates, *Phys. Rev. A* 91(4), 043604 (2015)
35. Z. F. Yu, A. X. Zhang, R. A. Tang, H. P. Xu, J. M. Gao, and J. K. Xue, Spin–orbit-coupling stabilization of a collapsing binary Bose–Einstein condensate, *Phys. Rev. A* 95(3), 033607 (2017)
36. T. Ozawa and G. Baym, Stability of ultracold atomic Bose condensates with Rashba spin–orbit coupling against quantum and thermal fluctuations, *Phys. Rev. Lett.* 109(2), 025301 (2012)
37. R. X. Zhong, Z. P. Chen, C. Q. Huang, Z. H. Luo, H. S. Tan, B. A. Malomed, and Y. Y. Li, Self-trapping under two-dimensional spin–orbit coupling and spatially growing repulsive nonlinearity, *Front. Phys.* 13(4), 130311 (2018)
38. Y. X. Yang, P. Gao, L. C. Zhao, and Z. Y. Yang, Kink-like breathers in Bose–Einstein condensates with helicoidal spin–orbit coupling, *Front. Phys.* 17(3), 32503 (2022)
39. Y. Han, X. Q. Luo, T. F. Li, and W. Zhang, Analytical double-unitary-transformation approach for strongly and periodically driven three-level systems, *Phys. Rev. A* 101(2), 022108 (2020)
40. M. Bukova, L, D. Alessioab, and A. Polkovnikova, Universal high-frequency behavior of periodically driven systems: From dynamical stabilization to Floquet engineering, *Adv. Phys.* 64, 139 (2015)
41. A. Eckardt, Atomic quantum gases in periodically driven optical lattices, *Rev. Mod. Phys.* 89(1), 011004 (2017)
42. Y. Zhang, G. Chen, and C. Zhang, Tunable Spin-orbit Coupling and Quantum Phase Transition in a Trapped Bose-Einstein Condensate, *Sci. Rep.* 3(1), 1937 (2013)
43. K. Jiménez-García, L. J. LeBlanc, R. A. Williams, M. C. Beeler, C. Qu, M. Gong, C. Zhang, and I. B. Spielman, Tunable spin–orbit coupling via strong driving in ultracold-atom systems, *Phys. Rev. Lett.* 114(12), 125301 (2015)
44. J. M. Gomez Llorente, and J. Plata, Periodic driving control of Raman-induced spin–orbit coupling in Bose–Einstein condensates: The heating mechanisms, *Phys. Rev. A* 93(6), 063633 (2016)
45. M. Salerno, F. Kh. Abdullaev, A. Gammal, and L. Tomio, Tunable spin–orbit-coupled Bose–Einstein condensates in deep optical lattices, *Phys. Rev. A* 94(4), 043602 (2016)
46. F. Kh. Abdullaev, M. Brtka, A. Gammal, and L. Tomio, Solitons and Josephson-type oscillations in Bose–Einstein condensates with spin–orbit coupling and time-varying Raman frequency, *Phys. Rev. A* 97(5), 053611 (2018)
47. X. W. Luo and C. W. Zhang, Tunable spin–orbit coupling and magnetic superstripe phase in a Bose–Einstein condensate, *Phys. Rev. A* 100(6), 063606 (2019)
48. J. C. Liang, Y. C. Zhang, C. Jiao, A. X. Zhang, and J. K. Xue, Ground-state phase and superfluidity of tunable spin–orbit-coupled Bose–Einstein condensates, *Phys. Rev. E* 103(2), 022204 (2021)
49. Z. Lin, Phase diagrams of periodically driven spin–orbit coupled ^{87}Rb and ^{23}Na Bose–Einstein condensates, *Ann. Phys.* 533(1), 2000194 (2021)
50. E. Kengne and W. M. Liu, Management of matter-wave solitons in Bose–Einstein condensates with time-dependent atomic scattering length in a time-dependent parabolic complex potential, *Phys. Rev. E* 98(1), 012204 (2018)
51. E. A. Donley, N. R. Claussen, S. L. Cornish, J. L. Roberts, E. A. Cornell, and C. E. Wieman, Dynamics of collapsing and exploding Bose–Einstein condensates, *Nature* 412(6844), 295 (2001)
52. Y. C. Xiong and L. Yin, Self-bound quantum droplet with internal stripe structure in one-dimensional spin–orbit-coupled Bose gas, *Chin. Phys. Lett.* 38(7), 070301 (2021)
53. R. Sachdeva, M. N. Tengstrand, and S. M. Reimann, Self-bound supersolid stripe phase in binary Bose–Einstein condensates, *Phys. Rev. A* 102(4), 043304 (2020)
54. J. Sanchez-Baena, J. Boronat, and F. Mazzanti, Supersolid striped droplets in a Raman spin–orbit-coupled system, *Phys. Rev. A* 102(5), 053308 (2020)